



Chitosan coating of BaTiO₃@ZnO:Yb heterostructures: synthesis and properties

S. Fuentes^{1,2} · J. León^{2,3} · J. L. Vega⁴ · S. Zenteno¹

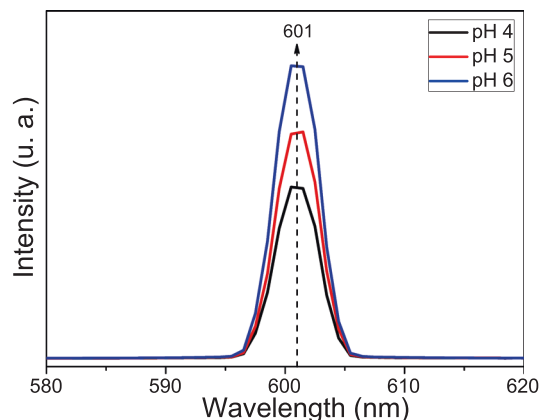
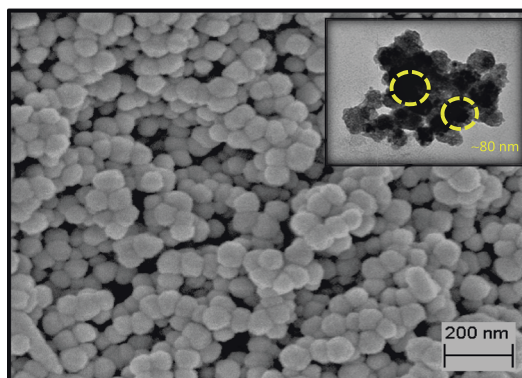
Received: 13 January 2020 / Accepted: 22 May 2020 / Published online: 2 June 2020
© Springer Science+Business Media, LLC, part of Springer Nature 2020

Abstract

In this study, BT@ZnO:Yb heterostructures prepared using the combined sol-gel-hydrothermal methods were coated with chitosan (Qo) to obtain a hybrid heterostructure [BT@ZnO:Yb]-Qo. The structure, particle morphology, luminescence properties, and cytotoxicity of the hybrid heterostructure are discussed. X-ray diffraction (XRD), scanning electron microscopy (SEM), transmission electron microscopy (TEM), Fourier transform infra-red (FT-IR) as well as Raman and photoluminescence spectra, were used for characterisation and monitoring of the heterostructure formation process. The results reveal the formation of the BT@ZnO:Yb heterostructure, and are consistent with the relative intensities and positions of peaks in the XRD spectra of BT and ZnO:Yb, with the average particle size of ~75 nm. Effective Qo coating was achieved and a narrow, well-defined, and high-intensity luminescence signal was detected at ~610 nm for all the analysed samples. In vitro studies suggested that treatment with 1 µg/ml BT@ZnO:Yb 3 mol% induced very low cytotoxicity on HeLa cells.

Graphical Abstract

The morphology of the [BT@ZnO:Yb]-Qo heterostructures shows that the Nps were uniformly distributed throughout the Qo matrix, with the average particle diameter of ~80 nm with the tennis-ball-like spheres after the incorporation of chitosan. The prepared hybrid heterostructures exhibited a narrow, well-defined, and high-intensity luminescence peak at ~610 nm for all the analysed samples, and low cytotoxicity at 1 µg/ml.



✉ S. Fuentes
sfuentes@ucn.cl

¹ Departamento de Ciencias Farmacéuticas, Facultad de Ciencias, Universidad Católica del Norte, Casilla, 1280 Antofagasta, Chile

² Center for the Development of Nanoscience and Nanotechnology, CEDENNA, Santiago, Chile

³ Department of Biomedicine, Laboratory of Biology of Reproduction, Faculty of Health Sciences, University of Antofagasta, 1240000 Antofagasta, Chile

⁴ Instituto Antofagasta, Universidad de Antofagasta, 1240000 Antofagasta, Chile

Keywords Oxide materials · Heterostructures · Yb-doping · PL spectra · Cytotoxicity

Highlights

- BaTiO₃@ZnO:Yb heterostructures can be obtained by the sol-gel-hydrothermal process.
- Effective heterostructures based on the coating with Qo, [BT@ZnO:Yb]-Qo, were synthesised with low cytotoxicity.
- The PL intensity depends on the pH of the dispersion medium.
- Ytterbium luminescence can be used in diagnostic imaging.

1 Introduction

Inorganic nanoparticles (NPs) are of particular interest for medical applications, owing to their remarkable performance in biological imaging, sensors, and gene and drug delivery, to name a few [1]. The advantages of inorganic NPs are attributed to their intrinsic properties, which include optical and superparamagnetic properties, on the scale of cells and even subcellular organelles [2]. Among such applications, immense attention has been devoted to materials that are capable of generating short-wavelength radiation from long-wavelength sources. One of the ways to achieve such conversion is by the second harmonic generation (SHG) [3]. In the SHG pathway, new frequencies are generated owing to the weakly wavelength-dependent hyperpolarisability of the underlying substance, and intense coherent excitation sources are required [4]. On the other hand, it is a second-order nonlinear optical process in which two photons, at frequency ω , that interact with a noncentrosymmetric medium, are combined to form a new photon with twice the energy of the initial individual photons, and therefore twice the frequency (2ω) and half the wavelength of the initial photons [3–5]. Compared with fluorescent probes, noncentrosymmetric NPs have several attractive properties, including the complete absence of bleaching and blinking, narrow emission bands, excitation-wavelength tunability, orientation retrieval capability, and coherent optical response [6, 7].

The SHG properties of several crystals have been reported, including those of BaTiO₃ [8, 9], ZnO [9, 10], KTiOPO₄ [11, 12], Sr_{0.6}Ba_{0.4}Nb₂O₆ [13], KNbO₃ [9, 14], HgI₂ [15], and LiNbO₃ [9, 16]. Barium titanate (BT), which presents a bright SHG signal even when the illumination intensities of the two photons are well below the tissue damage threshold, does not bleach or blink, can be excited with deeper-penetration long-wavelength light, and has a narrow multi-directional signal spectrum [8, 9]. On the other hand, zinc oxide (ZnO) is a widely used metal oxide for NPs, and its crystal structure is wurtzite, which contributes to its unique optoelectric properties [17]. ZnO is a wide band-gap semiconductor ($E_g = 3.37$ eV), with a large excitation binding energy (60 eV); it exhibits near-UV emission and possesses transparent conductivity and

piezoelectricity [17]. ZnO NPs have attracted significant interest owing to their good tissue adhesion properties, high ability, and strong antibacterial activity [18, 19].

The above-mentioned BT- and ZnO- NPs, however, are inefficient at entering cells without some form of functionalisation or conjugation, primarily owing to the negative surface charge of the NPs that prevents them from binding to negatively charged cell surfaces [20, 21]. Several macromolecules have been proposed as coating agents to protect and stabilise BT and ZnO NPs; these include Qo, chitin, alginate, hyaluronic acid, collagen, gelatine, polyurethane, polyethyleneimine, poly L-lactic-co-glycolic acid, polylactic acid, and polyvinyl alcohol [22–24]. Qo, in particular, is characterised by good biocompatibility, biodegradability, non-toxicity, and moisture-retention ability [25]. In addition, Qo is particularly noteworthy for the synthesis of metal NPs owing to its interaction with metal ions and metal oxide NPs. It is worth noting that chelation evenly disperses metal oxides throughout the Qo polymer [25, 26].

The objective of the current work was to propose a method for the synthesis of heterostructures based on inorganic NPs coated with Qo, specifically BT@ZnO:Yb, with the far-reaching goal of improving their intrinsic optical properties. The effect of pure and coated BT@ZnO:Yb NPs on the structural and morphological properties of heterostructures was studied. The chemo-physical properties and cytotoxicity of the synthesised hybrid heterostructures were evaluated.

2 Materials and methods

2.1 Materials

Barium chloride (BaCl₂, 99.9%), tetrabutyl titanate [(C₄H₉O)₄Ti, 98.0%], sodium hydroxide (NaOH, ≥98.0%), zinc chloride (ZnCl₂, 98.0%), ytterbium(III) chloride (YbCl₃·6H₂O, ≥99.9%), chitosan (low molecular weight), nitric acid (HNO₃, 65.0%), glacial acetic acid (CH₃COOH, 100.0%), hydrochloric acid (HCl, 37.0%), and 2-propanol (C₃H₈O, ≥99.8) were purchased from Sigma-Aldrich as starting materials.

2.2 Synthesis of ZnO:Yb NPs

ZnO:Yb NPs with $x = 0, 1, 3,$ and $5 \text{ mol}\%$ were synthesised by the sol-gel-hydrothermal process using zinc chloride (Merck) and ytterbium (III) chloride (Aldrich, $\geq 99.9\%$) as starting materials. The synthesis precursor of Yb-doped ZnO ($x \text{ mol}\%$) was obtained by dissolving 2.0 g of ZnCl_2 in distilled water and NaOH ($v:v = 1:1$). YbCl_3 was dissolved in a 0.7 M HNO_3 solution; the molar ratios of Yb^{3+} ions were $0, 1, 3,$ and $5 \text{ mol}\%$, respectively. The mixture was magnetically stirred for 2 h at $150 \text{ }^\circ\text{C}$ and transferred to a 20 mL Teflon-lined stainless steel reactor, which was sealed and heated at $195 \text{ }^\circ\text{C}$ for 48 h . Finally, the autoclave was cooled to room temperature under environmental conditions. The resulting precipitates were collected, centrifuged, washed with deionized water resin (DI), and dried at $95 \text{ }^\circ\text{C}$ after removing the remaining ions.

2.3 Synthesis of BT@ZnO:Yb NPs

BT@ZnO:Yb NPs were synthesised by the sol-gel-hydrothermal process using tetrabutyl titanate (TBT) and barium chloride (BaCl_2) as starting materials. In a typical procedure, solution (A) containing 1.5 mL of TBT was diluted with 20 mL of 2-propanol for 10 min to form a white solution, which was added dropwise at $60 \text{ }^\circ\text{C}$ for 3 h , while stirring, to solution (B), which contained 1.2 mL of HNO_3 in 10 mL of deionised water ($45 \text{ }^\circ\text{C}$). An aqueous solution (C) was prepared by dissolving BaCl_2 in 10 mL of deionised water. To prepare the BT precursor, solution (C) was added dropwise to solution (B). While stirring for 3 h at $80 \text{ }^\circ\text{C}$ in N_2 bubbling, NaOH was added, and white homogeneous colloidal barium titanium slurry was formed. This solution was transferred and mixed with previously synthesised 0.92 g of ZnO:Yb in the 20 mL Teflon-lined stainless steel reactor, sealed, and then heated at $200 \text{ }^\circ\text{C}$ for 48 h . At the end of the reaction, the autoclave was allowed to cool to room temperature. The as-synthesised white powder attached to the bottom and inner wall of the Teflon-lined container was collected, centrifuged, washed with deionized water resin (DI) and ethanol, and the remaining ions were removed; finally, the obtained powder was dried at $100 \text{ }^\circ\text{C}$ for 3 h under reduced pressure.

2.4 Synthesis of [BaTiO₃@ZnO:Yb]-Qo heterostructures

One gram of Qo, with low molecular weight, was dissolved in 100 mL of 1% glacial acetic acid and stirred for 24 h at room temperature. The resulting solution was successively filtered through coarse- and fine-fritted funnels and then micro-filtered in a Millipore system using, consecutively, membranes with pore sizes of $3.0, 0.45,$ and $0.2 \mu\text{m}$. To obtain the

[BT@ZnO:Yb]-Qo heterostructure, 10 mg of BT@ZnO:Yb was slowly added to 10 mL of the Qo solution. Next, the mixed solutions were transferred into a 100 mL flask, and the flask was put in an ultrasonic reactor. Ultrasonic vibrations were generated using an ultrasonic cleaner, at the frequency of $\sim 40 \text{ kHz}$ and power of 80 W , for 10 min . Finally, the pH of the solution was modified using HCl , under constant stirring, to obtain a colloidal suspension of [BT@ZnO:Yb]-Qo. The suspension was centrifuged at 4000 rpm for 10 min , to separate the solids from the solution. The synthesised precipitate was centrifugally separated and washed with deionized water resin (DI) and then dried at $100 \text{ }^\circ\text{C}$ for 3 h .

2.5 Cell culture

HeLa cell lines (derived from human cervical cancer) were grown in the Dulbecco modified Eagle medium (DMEM), containing 4.5 g/L glucose, penicillin/streptomycin (Gibco, Carlsbad, CA), supplemented with 10% of heat-inactivated foetal bovine serum (FBS), and maintained in a humidified incubator at $37 \text{ }^\circ\text{C}$ with $5\% \text{ CO}_2$, as described previously [27].

2.6 Viability assay

To determine the relative cell viability, we use the 3-(4,5-dimethyl-2-thiazoyl)-2,5-diphenyltetrazolium bromide (MTT) assay. The MTT assay is a colorimetric sensitive indicator of the cellular metabolic activity relies on the reduction of MTT, a yellow water-soluble tetrazolium dye, primarily by the mitochondrial dehydrogenases, to purple coloured formazan crystals. HeLa cells (3×10^4) were plated per well in a 24-well plate with the DMEM containing 10% FBS and incubated for 24 h at $37 \text{ }^\circ\text{C}$ with $5\% \text{ CO}_2$. Then, the culture medium was replaced with the DMEM containing 10% FBS, and the cells were treated with [BT@ZnO:Yb]-Qo NPs (3 or 5%), at concentrations of $1, 10, 200,$ and $500 \mu\text{g/mL}$. After a 24 h long exposure, the MTT (3-(4,5-dimethyl-2-thiazoyl)-2,5-diphenyltetrazolium bromide) reagent (0.3 mg/mL) was added to the wells, and the plates were incubated for 1 h at $37 \text{ }^\circ\text{C}$. After this incubation period, the medium was removed and $200 \mu\text{L}$ of DMSO was added to each well to dissolve the formed crystals; then, the plates were read immediately at 540 nm using a microplate spectrophotometer (Multiskan TM GO Thermo Scientific, Japan). Data were reported as averages over three independent experiments \pm standard error of mean, and were expressed as percent viability with respect to the solvent control. The data were fitted using a non-linear dose-response regression.

2.7 Characterisation

The morphology of the samples was examined using a field emission scanning electron microscope (SEM, Hitachi

Model SU5000) equipped with an energy-dispersive X-ray spectroscopy (EDX) detector. X-ray diffraction (XRD) data were acquired using a Siemens advanced D-8 diffractometer with $\text{CuK}\alpha$ radiation at 40 kV and 30 mA. Fourier transform infra-red (FT-IR) spectroscopy measurements were performed using a Perkin Elmer FRONTIER MIR/FIR apparatus. Raman spectra were recorded on a WITEC model CRC200, using a 5.5 mW laser with the wavelength of 514.5 nm. Photoluminescence (PL) emission spectra were recorded at room temperature using a the JASCO FP-6500 spectrofluorometer. In addition, the signal was optimised with the use of the 300 nm shortpass filter for the light beam coming from the excitation and the 420 nm longpass filter before the detector.

3 Results and discussion

The XRD patterns of pure ZnO, BT, ZnO:Yb, BT@ZnO:Yb, and [BT@ZnO:Yb]-Qo heterostructures are shown in Fig. 1. The XRD Bragg reflection was assigned to that of the typical hexagonal wurtzite structure for ZnO and ZnO:Yb 3 mol% (JCPDS Card no 36–1451 diffraction card) with

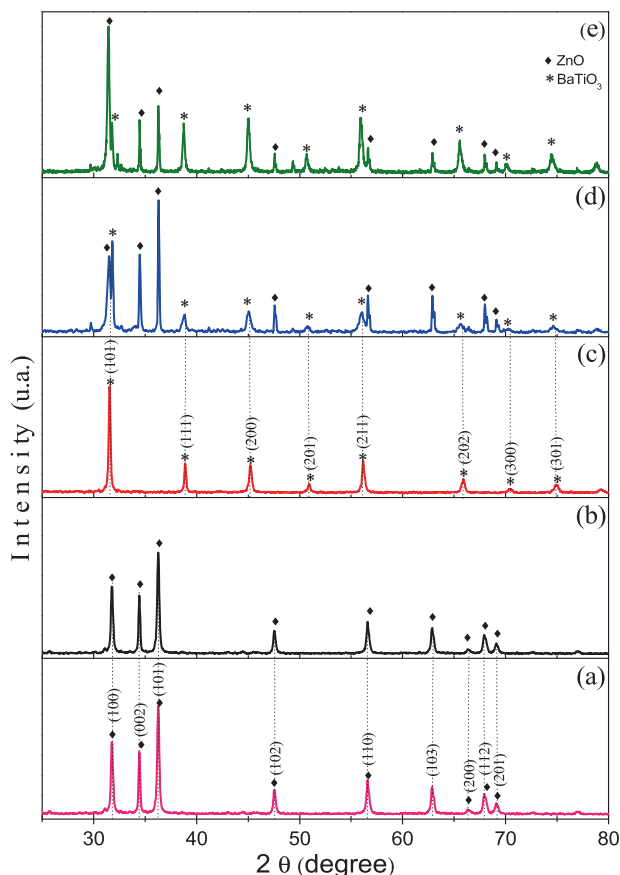


Fig. 1 XRD patterns of (a) ZnO; (b) ZnO:Yb 3% mol; (c) BT (d) BT@ZnO:Yb and (e) [BT@ZnO:Yb]-Qo 3% mol heterostructure

$P6_3mc$ space group are shown in Fig. 1 (a, b) respectively [28]. There were sharp and intensive diffraction peaks for the (100), (002), (101), (102), (110), (103), (200), (112), and (201) planes, while diffraction peaks associated with other phases were not observed. In Fig. 1(c), the characteristic peaks [i.e., (1 0 0), (11 0), (111), (2 0 0), (2 1 0), (2 11), and (2 2 0)], observed for the BT cubic lattice, are shown, in a good agreement with literature results [29] and the JCPDS 31-0174 card. The XRD patterns of the BT@ZnO:Yb 3 mol% heterostructure are demonstrated in Fig. 1(d), and the relative intensities and positions of peaks in the XRD patterns of the BT@ZnO:Yb 3 mol% heterostructure were consistent with the relative intensities and positions of peaks of the XRD patterns of BT and ZnO:Yb NPs. As the BT@ZnO:Yb 3 mol% heterostructures were introduced into the Qo matrix, the relative intensities and positions of peaks of the XRD patterns for [BT@ZnO:Yb]-Qo were consistent with the relative intensities and positions of peaks of the XRD patterns of BT@ZnO:Yb heterostructures, shown in Fig. 1(e). Moreover, a clear increase in the intensity of the peaks associated with the perovskite structure of the BT was observed, compared with the peaks of the wurtzite structure at ZnO:Yb 3% mol. This increase in intensity was associated with the use of the ultrasound technique for coating the polymer matrix, since it increased the extent of the disaggregation of the NPs.

The average particle size was estimated based on the (101) diffraction peak and the Scherrer equation, given by: $d = k\lambda/(\beta/\cos(\theta))$, where d is the particle size, $k \sim 1$ is the shape factor, $\lambda = 0.1540$ nm is the wavelength of the $\text{CuK}\alpha$ radiation, β is the full-width at half-maximum (FWHM), and θ is the diffraction angle. The average crystallite sizes for the pure ZnO, BT, ZnO:Yb, BT@ZnO:Yb 3 mol% and [BT@ZnO:Yb]-Qo heterostructures were ~ 68 , ~ 73 , ~ 69 , ~ 72 , and ~ 84 nm, respectively.

The morphologies of the ZnO, ZnO:Yb, BT@ZnO:Yb, and [BT@ZnO:Yb]-Qo heterostructures were examined using scanning electron microscopy (SEM) and transmission electron microscopy (TEM). The typical SEM and TEM images are shown in Fig. 2. Figure 2(a–c) show that the size and the morphology of the NPs are not uniform, with particles having rod-shaped morphology for pure ZnO. The NPs of ZnO:Yb (Fig. 2 b) show that the surface morphology is nearly identical to that of the undoped ZnO (Fig. 2a). The little variation in the shape and size of the ZnO:Yb NPs was associated with Yb^{3+} doping of the ZnO crystal structure, which affected the crystalline plane of growth [30]. The BT@ZnO:Yb NPs were less uniform and more spherical than those of ZnO:Yb (Fig. 2c). As shown in Fig. 2(d), tennis-ball-like spheres were formed after the incorporation of Qo into the BT@ZnO:Yb heterostructure. The inset of Fig. 2(d), showing the TEM image, reveals that the [BT@ZnO:Yb]-Qo heterostructures were uniformly

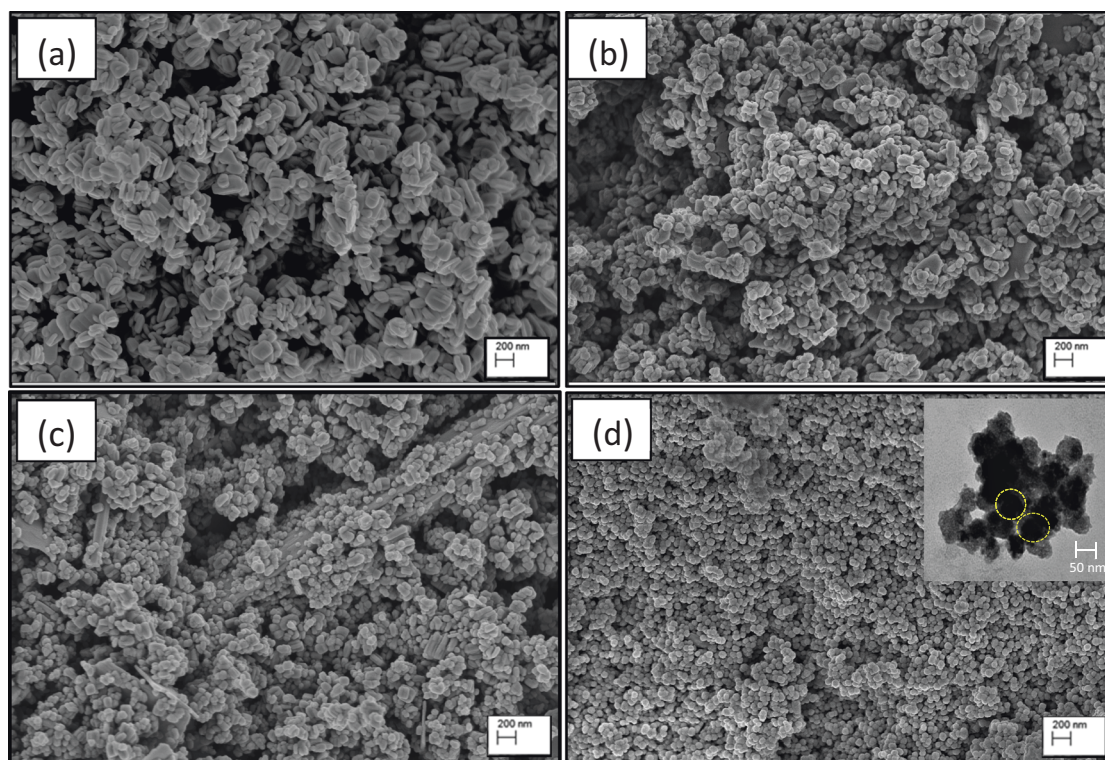


Fig. 2 SEM images of (a) ZnO; (b) ZnO:Yb; (c) BT@ZnO:Yb and (d) [BT@ZnO:Yb]-Qo 3% mol. The inset shows the TEM image of heterostructure

distributed throughout the Qo matrix, with the average particle diameter of ~ 80 nm.

This may be due to the application of ultrasonic vibration produces a rearrangement of superficial crystallites, altering the morphology and size of the heterostructure (these findings are consistent with the results of XRD patterns as previously discussed).

Zhang et al. [31], found that ultrasonic irradiation dramatically enhanced Ostwald ripening via acoustic cavitation induced turbulence (i.e., microstreaming and shock waves) in synthesised single crystalline gold nanobelts. The nanoparticle size decreased with increasing ultrasonic reaction times.

On the other hand, Qo plays a vital role in determining the particle size and stabilising. This might be owing to the large amount of Qo binding to the surfaces of the [BT@ZnO:Yb]-Qo heterostructures [32].

Figure 3 shows the FT-IR spectra for the (a) ZnO, (b) BT@ZnO:Yb, and (c) [BT@ZnO:Yb]-Qo NPs. In general, all of the characteristic peaks of Qo are present in the spectra of the [BT@ZnO:Yb]-Qo heterostructures (Fig. 3c). The broad band at ~ 3445 cm^{-1} is attributed to overlapping of the stretching vibration modes of O–H (lattice H_2O) and the vibration of the N–H groups of Qo. The C–H stretching vibrations of the CH_2 and CH_3 groups of the polymer backbone were observed at 2960, 2849, and 1381 cm^{-1} .

The band at 1622 cm^{-1} was assigned to the N–H bending vibration (amide I band). Finally, the sharp peak at 1080 cm^{-1} can be assigned to the C–O–C stretching in the glucosamine residue [33]. Regarding the naked ZnO NPs (Fig. 3a), the peaks at ~ 558 and ~ 434 cm^{-1} were assigned to the Zn–O stretching vibrations of the metal–oxygen bonds of the wurtzite structure [34]. The peak at 1380 cm^{-1} was associated with the stretching vibrations of the carbonate ions (CO_3^{2-}), corresponding to CO_2 and/or BaCO_3 produced as impurities in the synthesis process (Fig. 3b). The intensity of that band decreased after the Qo coating to obtain the [BT@ZnO:Yb]-Qo heterostructures. This confirms that the ultrasound method allowed to eliminate the impurities of BaCO_3 produced in the synthesis of BT@ZnO:Yb heterostructures, which agrees with the results shown in DRX.

The Raman spectra obtained at room temperature for the ZnO, BT, ZnO:Yb, and BT@ZnO:Yb NPs, are shown in Fig. 4. The Raman spectra of the ZnO (Fig. 4a) samples prepared can be assigned to the optical phonon modes of ZnO with the hexagonal wurtzite crystal structure belong to the space group $P6_3mc$ with two formula units in the primitive cell [35, 36]. In general, five characteristic Raman bands were present in the samples, at ~ 334 cm^{-1} [E_2 (TO)- E_2 (LO)], ~ 384 cm^{-1} [A_1 (TO)], ~ 402 cm^{-1} [E_1 (TO)], ~ 439 cm^{-1} associated with mode E_2 with the highest

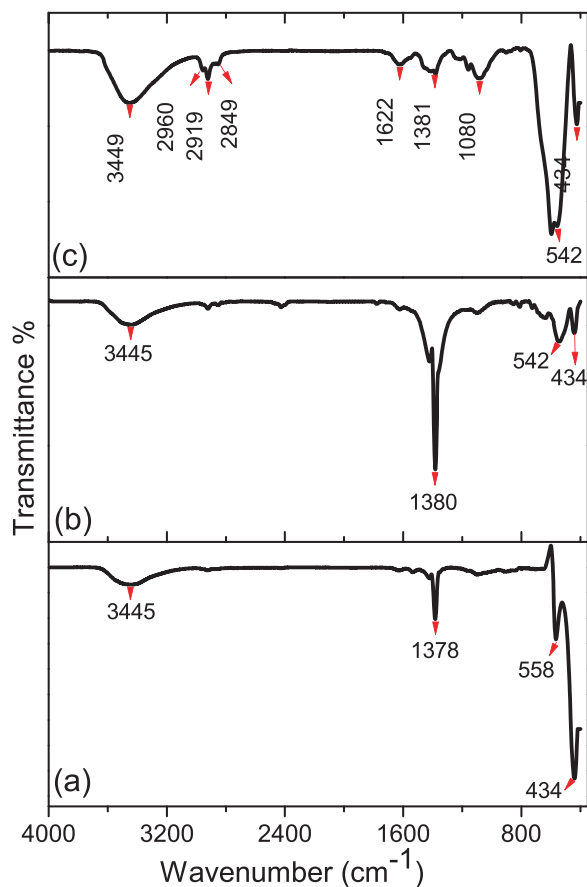


Fig. 3 FTIR spectra of (a) ZnO; (b) BT@ZnO:Yb and (c) [BT@ZnO:Yb]-Qo 3% mol heterostructure

intensity and $\sim 574 \text{ cm}^{-1}$ [E_1 (LO)]. The low E_2 mode (the peak at $\sim 100 \text{ cm}^{-1}$, named E_2^{low}) was associated with vibrations in the Zn sub-lattice, while the high E_2 mode (the mode at 439 cm^{-1} , named E_2^{high}) was associated mainly with the oxygen atom vibrations; it exhibited dominant intensity and was very sharp with respect to the other peaks, which indicated good crystallinity of the ZnO NPs structures [37]. In Fig. 4(b), the ZnO samples doped with Yb are very similar to the pure ZnO, with all the peaks' characteristics as mentioned above. The Raman spectra of BT (Fig. 4c) were similar to those obtained for the NPs of pure BT in a previous study [29]. They exhibited a characteristic Raman peak near 306 cm^{-1} (B1 mode), corresponding to the tetragonal BT phase, and contrary to the cubic symmetry observed by the XRD analysis, from which no first-order Raman activity was expected [38]. In general, four characteristic Raman bands were present in the analysed samples, one at $\sim 307 \text{ cm}^{-1}$ [B1, E(TO + LO)], and three broad bands near $\sim 254 \text{ cm}^{-1}$ [A1(TO)], $\sim 510 \text{ cm}^{-1}$ [A1, E(TO)], and $\sim 720 \text{ cm}^{-1}$ [A1, E(LO)]. The Raman spectrum of the BT@ZnO:Yb NPs, shown in Fig. 4(c), confirm the presence of a heterogeneous mixture of crystalline structures, both hexagonal wurtzite of ZnO and perovskite of BT. The latter

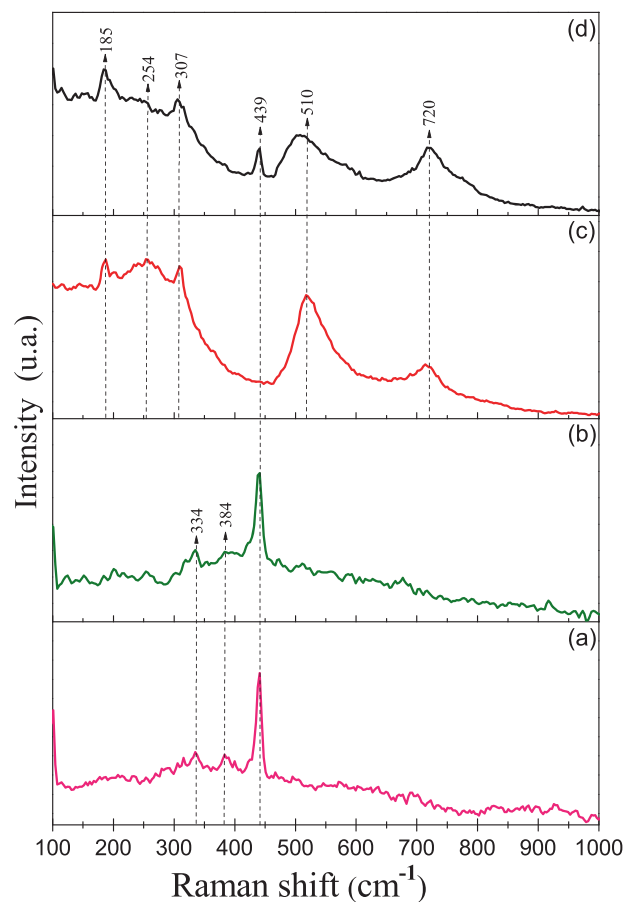


Fig. 4 Raman spectra of (a) ZnO; (b) ZnO:Yb 3% mol; (c) BT and (d) BT@ZnO:Yb 3% mol nanoparticles

Table 1 The z-average diameter, PDI, and Zeta potential of [BT@ZnO:Yb]-Qo 3% mol heterostructure

pH	Zeta potential (mV)	PDI	Z-average diameter (nm)
4	43.3	0.27	237.9
5	39.9	0.26	257.2
6	24.2	0.27	215.7

also presents a coexistence of phases, where the tetragonal phase (space group, P4 mm) predominates over the cubic phase (space group, Pm3m).

The [BT@ZnO:Yb]-Qo heterostructure at different pH were characterised for zeta potentials and z-average diameter (Table 1). The zeta potential of the heterostructures became less positive with increasing the pH value, owing to the reduction in the number of positively charged amine groups on the Qo. According to reports, suspensions with higher colloidal stability exhibit lower pH values at zeta potentials $< 40 \text{ mV}$, which indicates an effective coating of the associated heterostructures. Based on our results, we choose to work at $\text{pH} = 5$ in subsequent experiments, because it meets the ideal potential

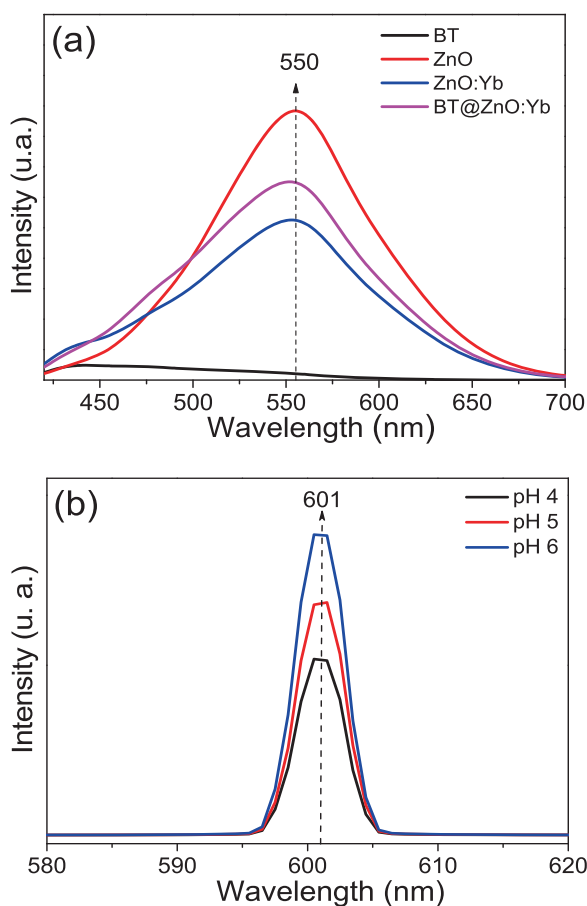


Fig. 5 Luminescence spectra of (a) the powder samples and (b) [BT@ZnO:Yb]-Qo 3% mol heterostructure with different pH values. The spectra were measured with an excitation wavelength of 300 nm

(± 30 mV) and is the closest to the physiologically relevant pH range [39]. The measured z -average diameter for the studied range of pH values yielded aggregates with sizes in the 200–280 nm range. The similarity of these results implies that the NP size is not pH-dependent. However, the polydispersity index (PDI) remained in the 0.2–0.3 range, for the three studied pH values (Table 1) and was characteristic of samples with moderate polydispersity (0.1–0.4) [40].

Figure 5(a) displays the luminescence spectra of the powder samples. The characteristic emission of ZnO is observed in the visible range centred at 555 nm, associated with deep-level electronic transitions of oxygen vacancies and structure defects [33, 41]. The doping of ZnO with Yb^{3+} and the subsequent attachment with BT induces additional defects in the structure, decreasing the signal intensity [42]. Figure 5(b) shows the luminescence spectra of the suspensions of [BT@ZnO:Yb]-Qo heterostructures for pH = 4, 5, and 6. A narrow, well-defined, and high-intensity luminescence peak was detected at ~ 610 nm for all of the analysed samples. In addition, the signal strength

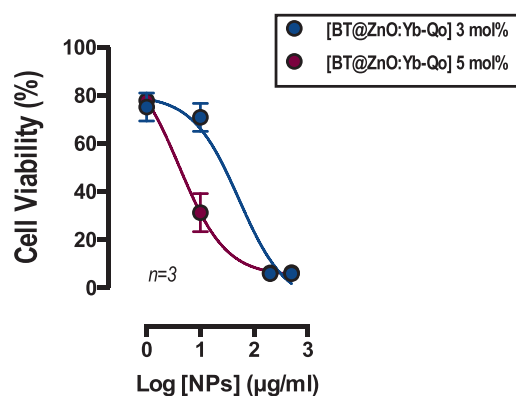


Fig. 6 Effect of [BT@ZnO:Yb]-Qo nanoparticles on HeLa cell viability. Cells were treated with vehicle (DMEM) or nanoparticles (NPs) at different doses (1, 10, 200, and 500 $\mu\text{g/ml}$) for 24 h and cell viability was analysed by MTT assay. To determine the cell viability, we calculated percent viability as $\% \text{ viability} = [(\text{Optical density of treated cell} - \text{Optical density of blank}) / (\text{Optical density of vehicle control} - \text{Optical density of blank}) \times 100]$. The results were adjusted to a non-linear dose-response regression and data are shown as mean \pm standard error ($n = 3$)

increased with increasing pH. Therefore, the luminescence intensity depends on the pH of the dispersion medium. This result was associated with the combination of the heterostructures coated with Qo, [BT@ZnO:Yb]-Qo; these results have not been published yet and require further researching. However, existing reports indicate that the luminescence signal at ~ 600 nm is associated with a change in the energy band structure induced by doping [32]. Yb^{3+} doping has also been reported to increase the number of surface states, and to increase the number of defects and oxygen vacancies in ZnO [32, 43].

To monitor the effect of the [BT@ZnO:Yb]-Qo NPs on the viability of cells, an MTT assay was studied. We used HeLa cell lines because a significant amount of toxicity data is available for comparison [10, 38, 44–46]. The results showed that treatment at the concentration of 1 $\mu\text{g/ml}$ [BT@ZnO:Yb]-Qo induced very low cytotoxicity, with relative cell viability values of $75.13 \pm 0.5\%$ for 3 mol% and $77.81 \pm 0.3\%$ for 5 mol% (Fig. 6). Previous studies have shown that BT NPs also exhibit low toxicity [39] and ZnO NPs do not cause cytotoxicity at concentrations between 50–150 $\mu\text{g/ml}$ for HeLa cells [10]. However, treatment at concentrations above 200 $\mu\text{g/ml}$ caused high cytotoxicity, with cell viability values of 6.12 ± 0.1 and $5.86 \pm 0.1\%$ for 3 and 5 mol%, respectively (Fig. 6). The median lethal doses (LD_{50}) were 52.63 ± 0.25 and 4.07 ± 0.14 $\mu\text{g/ml}$ for 3 and 5 mol%, respectively. For HeLa cells, previous studies reported cytotoxicity in the 16–42 $\mu\text{g/ml}$ range [39]. Our results are consistent with these reports, even though our [BT@ZnO:Yb]-Qo-3 mol% NPs are less toxic, with the LD_{50} of 52.63 $\mu\text{g/ml}$.

4 Conclusions

The purpose of this study was to investigate the synthesis of heterostructures based on the coating of inorganic particles with Qo ([BT@ZnO:Yb]-Qo). The heterostructures were synthesised using the sol-gel-hydrothermal technique. The chemical, physical, and biological properties of the synthesised heterostructures were examined using conventional methods. The heterostructures were characterised using XRD, SEM, TEM, FT-IR, Raman, and photoluminescence spectra. The XRD analysis revealed the polycrystalline nature of BT@ZnO:Yb NPs, with the average crystallite size of ~75 nm. The SEM analysis revealed rod-shaped small granules, with sizes in the 70–120 nm range. The FT-IR analysis confirmed the functional groups present in the organic material used as coating, as well as the metal–oxygen formations. The prepared hybrid heterostructures exhibited a narrow, well-defined, and high-intensity luminescence peak at ~610 nm for all the analysed samples, and low cytotoxicity at 1 µg/ml.

Acknowledgements This work has been partially financed by Basal Financing Program CONICYT, AFB180001 (CEDENNA). SF thanks to FONDEQUIP project EQM140044 and Scientific Equipment Unit – MAINI of Universidad Católica del Norte. This work was partially supported by a MINEDUC-UA project code ANT 1755 (to JLV).

Compliance with ethical standards

Conflict of interest The authors declare that they have no conflict of interest.

Publisher's note Springer Nature remains neutral with regard to jurisdictional claims in published maps and institutional affiliations.

References

1. Tonga GY, Moyano DF, Kim CS, Vincent M (2014) Inorganic nanoparticles for therapeutic delivery: Trials, tribulations and promise. *Curr Opin Colloid Interface Sci* 19:49–55
2. Krishna KS, Li Y, Li S, Kuma SSR (2013) Lab-on-a-chip synthesis of inorganic nanomaterials and quantum dots for biomedical applications. *Adv Drug Deliv Rev* 65:1470–1495
3. Gamelin DR (2001) Upconversion processes in transition metal and rare earth metal systems. In: Y. H (ed.) *Transition metal and rare earth compounds*. Springer, Germany, pp 1–56
4. Boyd R (2003) *Nonlinear optics*, 2nd edn. Academic Press, NY, USA
5. Hasan SB, Lederer F, Rockstuhl C (2014) Nonlinear plasmonic antennas. *Mater Today* 17:478–485
6. Baumner R, Bonacina L, Enderlein J, Extermann J, Fricke-Begemann T, Marowsky G, Wolf JP (2010) Evanescent-field-induced second harmonic generation by noncentrosymmetric nanoparticles. *Opt Express* 18:23218–23225
7. Chen WL, Hu PS, Ghazaryan A, Chen SJ, Tsai TH, Dong CY (2012) Quantitative analysis of multiphoton excitation autofluorescence and second harmonic generation imaging for medical diagnosis. *Comput Med Imaging Graph* 36:519–526
8. Chin H-A, Mao S, Meng F, Ohemeng KK, Purohit PK, Wagner S, McAlpine MC (2016) A flexible barium strontium titanate photodetector array. *Extrem Mech Lett* 8:47–54
9. Staedler D, Magouroux T, Hadji R, Joulaud C, Extermann J, Schwung S, Passemard S, Kasparian C, Clarke G, Germann M, Le Dantec R, Mugnier Y, Rytz D, Ciepiewski D, Galez C, Gerber-Lemaire S, Juillerat-Jeanneret L, Bonacina L, Wolf JP (2012) Harmonic nanocrystals for biolabeling: a survey of optical properties and biocompatibility. *ACS Nano* 6:2542–2549
10. Gu B, Pliss A, Kuzmin AN, Baev A, Ohulchansky TY, Damasoa JA, Yong KT, Wen S, Prasad PN (2016) In-situ second harmonic generation by cancer cell targeting ZnO nanocrystals to effect photodynamic action in subcellular space. *Biomaterials* 104:78–86
11. Dong N, Yao Y, Jia Y, Chen F, Vanga SK, Bettiol AA, Lu Q (2012) Buried channel waveguides in KTiOPO₄ nonlinear crystal fabricated by focused He⁺ beam writing. *Opt Mater* 35:184–186
12. Fontana MD, Abarkan M, Salvestrini JP (2014) Calculation of the dispersion of the electro-optical and second harmonic coefficients from the refractive index dispersion. *Opt Mater* 36:764–768
13. Ladj R, Magouroux T, Eissa M, Dubled M, Mugnier Y, Dantec RL, Galez C, Valour J-P, Fessi H, Elaissari A (2013) Aminodextran-coated potassium niobate (KNbO₃) nanocrystals for second harmonic bio-imaging. *Colloid Surf A* 439:131–137
14. Wang Y, Chen Z, Ye Z, Huang JY (2012) Synthesis and second harmonic generation response of KNbO₃ nanoneedles. *J Cryst Growth* 341:42–45
15. Shi X, Ma Z, He C, Wu K (2014) Strong SHG responses predicted in binary metal halide crystal HgI₂. *Chem Phys Lett* 608:219–223
16. Yadav TK, Singh AK, Kumar K, Yadav RA (2011) Luminescence and second harmonic generation in Eu³⁺/Eu²⁺ embedded B₂O₃:LiNbO₃ non-linear glass-ceramics. *Opt Mater* 33:1732–1736
17. Shohanya BG, Zak AK (2020) Doped ZnO nanostructures with selected elements-structural, morphology and optical properties: a review. *Ceram Int* 46:5507–5520
18. Mirzaei H, Darroudi M (2017) Zinc oxide nanoparticles: Biological synthesis and biomedical applications. *Ceram Int* 43:907–914
19. Özgür Ü, Alivov YI, Liu C, Teke A, Reshchikov MA, Doğan S, Avrutin V, Cho SJ, Morkoç H (2005) A comprehensive review of ZnO materials and devices. *J Appl Phys* 98:041301
20. Giner-Casares JJ, Henriksen-Lacey M, Coronado-Puchau M, Liz-Marzán LM (2016) Inorganic nanoparticles for biomedicine: where materials scientists meet medical research. *Mater Today* 19:19–28
21. Hernandez ME, Rembao JD, Hernandez-Baltazar D, Castillo-Rodriguez RA, Tellez-Lopez VM, Flores-Martinez YM, Orozco-Barrios CE, Rubio HA, Sanchez-Garcia A, Ayala-Davila J, Arango-Rodriguez ML, Pavon L, Mejia-Castillo T, Forgez P, Martinez-Fong D (2014) Safety of the intravenous administration of neurotensin-polyplex nanoparticles in BALB/c mice. *Nanomed-Nanotechnol* 10:745–754
22. Archana D, Singh BK, Dutta J, Dutta PK (2015) Chitosan-PVP-nano silver oxide wound dressing: in vitro and in vivo evaluation. *Int J Biol Macromol* 73:49–57
23. Meshram JV, Koli VB, Phadatare MR, Pawar SH (2017) Antimicrobial surfaces: An approach for deposition of ZnO nanoparticles on PVA-Gelatin composite film by screen printing technique. *Mater Sci Eng C Mater Biol Appl* 73:257–266
24. Wang X, Chang J, Wu C (2018) Bioactive inorganic/organic nanocomposites for wound healing. *Appl Mat Today* 11:308–319
25. Kong M, Chen XG, Xing K, Park HJ (2010) Antimicrobial properties of chitosan and mode of action: a state of the art review. *Int J Food Microbiol* 144:51–63
26. Bernkop-Schnurch A, Dunnhaupt S (2012) Chitosan-based drug delivery systems. *Eur J Pharm Biopharm* 81:463–469

27. Barria I, Guiza J, Cifuentes F, Zamorano P, Saez JC, Gonzalez J, Vega JL (2018) Trypanosoma cruzi Infection Induces Pannexin-1 Channel Opening in Cardiac Myocytes. *Am J Trop Med Hyg* 98:105–112
28. McMurdie H, Morris M, Evans E, Paretzkin B, Wong-Ng W, Hubbard C (1986) Standard X-Ray Diffraction Powder Patterns from The JCPDS Research Associateship. *Powder Diffr* 1:265–275
29. Fuentes S, Zárate RA, Chávez E, Muñoz P, Ayala M, Espinoza-González R, Leyton P (2010) Synthesis and characterization of BaTiO₃ nanoparticles in oxygen atmosphere. *J Alloy Compd* 505:568–572
30. Goel S, Kumar B (2020) A review on piezo-/ferro-electric properties of morphologically diverse ZnO nanostructures. *J Alloy Compd* 816:152491–152523
31. Zhang J, Du J, Han B, Liu Z, Jiang T, Zhang Z (2006) Sonochemical formation of single-crystalline gold nanobelts. *Angew Chem* 118:1134–1137
32. Saeed Sel S, El-Moll MM, Hassan ML, Bakir E, Abdel-Mottaleb MM, Abdel-Mottaleb MS (2014) Novel chitosan-ZnO based nanocomposites as luminescent tags for cellulosic materials. *Carbohydr Polym* 99:817–824
33. Magesh G, Bhoopathi G, Nithya N, Arun AP, Ranjith Kumar E (2018) Tuning effect of polysaccharide Chitosan on structural, morphological, optical and photoluminescence properties of ZnO nanoparticles. *Superlattices Microstruct* 117:36–45
34. Toiserkani H (2015) Fabrication and characterization chitosan/functionalized zinc oxide bionanocomposites and study of their antibacterial activity. *Compos Interfaces* 23:175–189
35. Damen TC, Porto SPS, Tell B (1966) Raman Effect in Zinc Oxide. *Phys Rev* 142:570–574
36. Jaramillo AF, Baez-Cruz R, Montoya LF, Medinam C, Pérez-Tijerina E, Salazar F, Rojas D, Melendrez MF (2017) Estimation of the surface interaction mechanism of ZnO nanoparticles modified with organosilane groups by Raman Spectroscopy. *Ceram Int* 43:11838–11847
37. Zolfaghari M (2019) Propose for Raman mode position for Mn-doped ZnO nanoparticles. *Phys B* 555:1–8
38. Tenne DA, Xi X (2008) Raman Spectroscopy of Ferroelectric Thin Films and Superlattices. *J Am Ceram Soc* 91:1820–1834
39. Dempsey C, Lee I, Cowan KR, Suh J (2013) Coating barium titanate nanoparticles with polyethylenimine improves cellular uptake and allows for coupled imaging and gene delivery. *Colloids Surf B* 112:108–112
40. Gambinossi F, Mylon SE, Ferri JK (2015) Aggregation kinetics and colloidal stability of functionalized nanoparticles. *Adv Colloid Interface Sci* 222:332–349
41. Karunakaran C, Vinayagamoorthy P, Jayabharathi J (2014) Optical, electrical, and photocatalytic properties of polyethylene glycol-assisted sol-gel synthesized BaTiO₃@ZnO core-shell nanoparticles. *Powder Technol* 254:480–487
42. Seid ET, Dejene FB, Kroon RE (2019) Synthesis, characterization and influence of pH on indium doped zinc oxide nanostructures. *Ceram Int* 45:24269–24278
43. Kanamori T, Han Y, Nagao D, Kamezawa N, Ishii H, Konno M (2016) Luminescence enhancement of ZnO-poly(methylmethacrylate) nanocomposite films by incorporation of crystalline BaTiO₃ nanoparticles. *Mater Sci Eng B* 211:173–177
44. Cardoso Avila PE, Rangel Mendoza A, Pichardo Molina JL, Flores Villavicencio LL, Castruita Dominguez JP, Chilakapati MK, Sabanero Lopez M (2017) Biological response of HeLa cells to gold nanoparticles coated with organic molecules. *Toxicol Vitro* 42:114–122
45. Khan JA, Pillai B, Das TK, Singh Y, Maiti S (2007) Molecular effects of uptake of gold nanoparticles in HeLa cells. *Chembiochem* 8:1237–1240
46. Lee E, Jeon H, Lee M, Ryu J, Kang C, Kim S, Jung J, Kwon Y (2019) Molecular origin of AuNPs-induced cytotoxicity and mechanistic study. *Sci Rep* 9:2494–2499